JACS
JOURNAL OF THE AMERICAN CHEMICAL SOCIETY
Article
pubs.acs.org/JACS

Two-Dimensional Mineral $[Pb_2BiS_3][AuTe_2]$: High-Mobility Charge Carriers in Single-Atom-Thick Layers

Lei Fang,*[,†,∥] Jino Im,[‡] Constantinos C. Stoumpos,[†,∥] Fengyuan Shi,[§] Vinayak Dravid,[§] Maxime Leroux,[∥] Arthur J. Freeman,[‡] Wai-Kwong Kwok,[∥] Duck Young Chung,[∥] and Mercouri Kanatzidis*[,†,∥]

[†]Department of Chemistry, [‡]Department of Physics and Astronomy, and [§]Department of Materials Science and Engineering, Northwestern University, Evanston, Illinois 60208, United States

[∥]Materials Science Division, Argonne National Laboratory, Argonne, Illinois 60439, United States

Supporting Information

ABSTRACT: Two-dimensional (2D) electronic systems are of wide interest due to their richness in chemical and physical phenomena and potential for technological applications. Here we report that $[Pb_2BiS_3][AuTe_2]$, known as the naturally occurring mineral buckhornite, hosts 2D carriers in single-atom-thick layers. The structure is composed of stacking layers of weakly coupled $[Pb_2BiS_3]$ and $[AuTe_2]$ sheets. The insulating $[Pb_2BiS_3]$ sheet inhibits interlayer charge hopping and confines the carriers in the basal plane of the single-atom-thick $[AuTe_2]$ layer. Magneto-transport measurements on synthesized samples and theoretical calculations show that $[Pb_2BiS_3][AuTe_2]$ is a multiband semimetal with a compensated density of electrons and holes, which exhibits a high hole carrier mobility of ~1360 $cm^2/(V\ s)$. This material possesses an extremely large anisotropy, $\Gamma = \rho_c/\rho_{ab} \approx 10^4$, comparable to those of the benchmark 2D materials graphite and $Bi_2Sr_2CaCu_2O_{6+\delta}$. The electronic structure features linear band dispersion at the Fermi level and ultrahigh Fermi velocities of 10^6 m/s, which are virtually identical to those of graphene. The weak interlayer coupling gives rise to the highly cleavable property of the single crystal specimens. Our results provide a novel candidate for a monolayer platform to investigate emerging electronic properties.

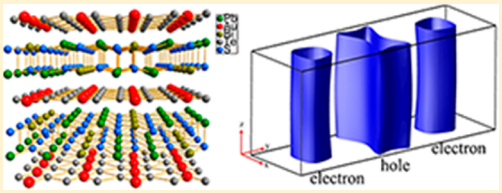

INTRODUCTION

Studies on two-dimensional electronic systems constitute one of the most intense activities in modern scientific research. Benchmark materials, such as graphene, 2D electron gas, and transition-metal dichalcogenides, have largely expanded the frontiers of low-dimensional physics and provide numerous opportunities to develop innovative technologies for microelectronics applications.[1−3] Currently, exploring layered materials featuring van der Waals bonding has become of great interest in considering novel 2D systems, such as, for instance, the record-high thermoelectric figure of merit recently discovered in the layered binary compound SnSe.[4] In addition to this focused direction of van der Waals-type layered structures, complex layered compounds composed of multiple building blocks also feature fascinating physical behavior. Examples include the novel interface topological insulating states in $[PbSe]_5[Bi_2Se_3]_6$, the ultralow thermal conductivity in the semiconducting heterostructure $[Tl_4Sb_6Se_{10}][Sn_5Sb_2Se_{14}]$, the ferecrystalline compounds $(PbSe)_m(MoSe_2)_n$, and the high-temperature superconductor $Bi_2Sr_2CaCu_2O_8$.[5,6] In this study, we introduce a layered heterostructure material, $[Pb_2BiS_3]$-$[AuTe_2]$, in which charge carriers are naturally confined in single-atom-thick layers of $AuTe_2$. This phase is known as a naturally occurring mineral referred to as buckhornite, but our studies were performed on synthesized specimens.[7] Its structure has orthorhombic symmetry and alternating layers of $[Pb_2BiS_3]$ and $[AuTe_2]$.[7,8] However, the reported structure was not adequately refined, and the properties of this mineral remained unknown. Here, we report an accurate structure determination using single crystal X-ray diffraction and transmission electron microscopy (TEM) derived from synthesized samples. We also report a variety of novel electronic properties determined by magneto-transport measurements and theoretical investigations that show that $[Pb_2BiS_3][AuTe_2]$ is a 2D semimetal with compensated concentrations of electrons and holes that exhibits high carrier mobility, extremely large anisotropy, and ultrahigh Fermi velocities.

RESULTS AND DISCUSSION

The structure of $[Pb_2BiS_3][AuTe_2]$ is shown in Figure 1a, with alternating stacks of the building blocks $[Pb_2BiS_3]$ and $[AuTe_2]$ along the *c*-axis. This structure is charge-balanced as $[Pb_2BiS_3]^+[AuTe_2]^-$, given the valence states are +2, +3, and +3 for Pb, Bi, and Au, respectively. The $[Pb_2BiS_3]$ sheet is distorted, likely due to the strain from the mismatch with the $[AuTe_2]$ lattice. The $[AuTe_2]$ slab is weakly bonded to the $[Pb_2BiS_3]$ sheet and virtually flat in the basal plane. A primary feature of the $[AuTe_2]$ slab is its single-atom thickness, analogous to graphene and hexagonal boron nitride.[1,9] Figure 1b displays a single planar $[AuTe_2]$ slab. Each Au atom has square planar bonding to four Te atoms and forms chains along the *b*-axis. The $[AuTe_2]$ chains are arranged side-by-side and

Received: November 4, 2014
Published: January 21, 2015

DOI: 10.1021/ja5111688
J. Am. Chem. Soc. 2015, 137, 2311−2317

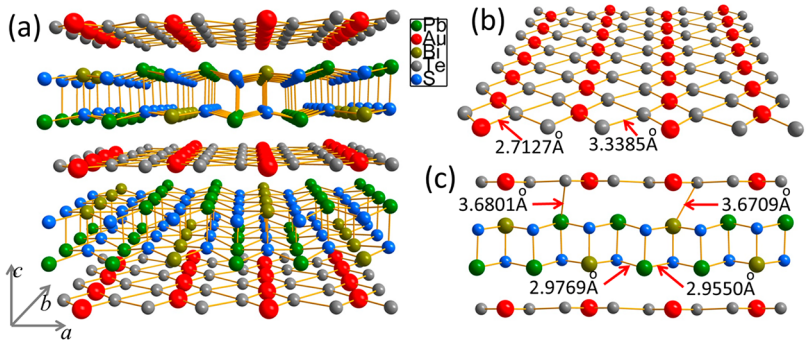

Figure 1. (a) Structure of $[Pb_2BiS_3][AuTe_2]$. (b) The $[AuTe_2]$ structure is made of parallel $AuTe_2$ chains that are single-atom-thick and analogous to graphene. The chains interact via interchain Te···Te bonding. (c) A side-view of the structure. As shown by the arrows between the two layers, the long chemical bonds indicate a weak interlayer coupling.

interact with one another via significant Te···Te interactions at 3.3385(28) Å. Figure 1c delineates the side view of two unit cells of $[Pb_2BiS_3][AuTe_2]$. The $[Pb_2BiS_3]$ and $[AuTe_2]$ are connected by long chemical bonds, for instance, the 3.6709(37) Å Pb−Te bond and 3.6801(27) Å Bi−Te bonds as resolved from our structure refinement. The weak interlayer coupling gives rise to the cleavable property of the $[Pb_2BiS_3][AuTe_2]$ crystal similar to layered solids that feature van der Waals bonds, e.g., graphite and MoS_2.[10] Exfoliating bulk crystals $[Pb_2BiS_3][AuTe_2]$ via the standard Scotch tape method on 300 nm SiO_2/Si substrate can successfully lead to ultrathin crystals that show sea-green contrast under visible light (see the inset of Figure 2b). This is different from the golden color of the bulk crystal section in the same image. The thickness of the thinnest part of the crystal is estimated at ∼10 nm by using the well-defined color-thickness relation of MoS_2 nanocrystals.[10] More

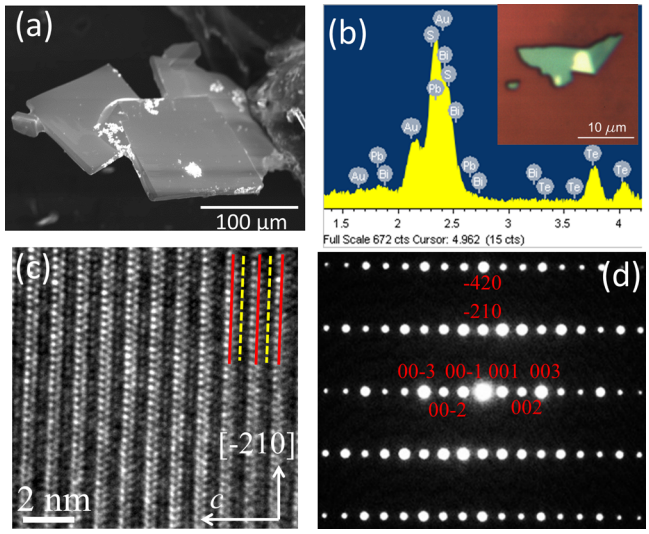

Figure 2. (a) SEM image of crystals of $[Pb_2BiS_3][AuTe_2]$. (b) EDS indicates a chemical composition of $Pb_{2.1}Bi_{1.09}S_{3.28}Au_{1.2}Te_{3.28}$, consistent with the ideal composition. The inset is an optical image of a cleaved crystal that shows sea-green pigment in the thinner layer and golden color in the thicker part. The thickness of the thinnest part of the crystal is approximately 10 nm. (c) The high-resolution TEM image along the [120] orientation shows that one slice of atom (highlighted by the yellow dashed line) consecutively aligns with a two-atom-thick slab (represented by the red solid line). (d) The corresponding selected area electron diffraction pattern of part c. The red numbers are the *hkl* index using the *Pmmn* space group.

detailed investigations of the thickness limit and nanocrystals' surface morphology will be reported elsewhere. Moreover, our structure determination suggests that a further thickness reduction to 1−2 nm may be possible. The interlayer distance between building blocks $[Pb_2BiS_3]$ and $[AuTe_2]$ is 3.6709 Å, greater than that of prototypical 2D materials like graphite, MoS_2, and $Bi_2Sr_2CaCu_2O_8$. The van der Waals bond length of graphite and MoS_2 are 3.3705 and 3.4881 Å, respectively.[1,3] For $Bi_2Sr_2CaCu_2O_8$, crystal cleavage happens between two neighboring $[Bi_2O_2]$ planes. The nearest bond between the two $[Bi_2O_2]$ planes is 3.4084 Å long.[6] It is known that a materials' bond strength is inversely proportional to the bond length. In this regard, the interlayer coupling strength of $[Pb_2BiS_3][AuTe_2]$ should be comparable to those of these notable 2D materials, which enables the generation of monolayers. Since the bonding between $[Pb_2BiS_3]$ and $[AuTe_2]$ is different than the van der Waals type of other 2D systems, direct comparisons should be made with caution. However, the weak interlayer coupling in $[Pb_2BiS_3][AuTe_2]$ is still able to produce good cleaving properties.

The crystal data and structure refinement details are listed in Table 1. Our refinement is more precise than the original reports. For instance, the "final *R* indices" and "goodness of fit" in our studies are 0.0632 and 1.053, respectively, and are much smaller than the values 0.101 and 1.38 in ref 7. High-resolution TEM investigations were performed in order to unambiguously determine the structure and to confirm the single-atom-thick $[AuTe_2]$ layer. Figure 2c is an atomic-resolved TEM image of $[Pb_2BiS_3][AuTe_2]$ crystal along [120] zone axis, which clearly shows that one slice of atoms is sandwiched by two thicker layers. The thicker layers, showing with greater brightness in the TEM image, are attributed to $[Pb_2BiS_3]$, and the layer between the two brighter atomic columns is $[AuTe_2]$. Figure 2d displays a selected area of the electron diffraction pattern, and the corresponding *hkl* indices which are fully consistent with our X-ray structure determination.

In order to gain a deeper understanding of this material, we performed first-principles electronic structure calculations.[11] The energy dispersion spectrum (Figure 3a) shows bands crossing the Fermi level, pointing to the metallic ground state of $[Pb_2BiS_3][AuTe_2]$. A hole pocket near X-Γ and two electron pockets near Γ-Y and T-Z can be clearly identified at the Fermi level. These pockets arise from the d-orbitals of Au and the p-orbitals of Te. Figure 3b is a plot of the density of states (DOS) with an energy cutoff ±4 eV. The DOS near the Fermi energy (E_F) is mainly associated with the Te orbitals. The spectral weight from Au is also evident. However, the contributions of

DOI: 10.1021/ja5111688
J. Am. Chem. Soc. 2015, 137, 2311−2317

Table 1. Crystal Data and Structure Refinement for $[Pb_2BiS_3][AuTe_2]$

empirical formula	$Pb_2BiS_3AuTe_2$	
formula weight	1171.71	
temperature	293(2) K	
wavelength	0.71073 Å	
crystal system	orthorhombic	
space group	*Pmmn*	
unit cell dimensions	a = 12.3722(16) Å	α = 90°
	b = 4.0997(7) Å	β = 90°
	c = 9.3435(14) Å	γ = 90°
volume	473.92(12) Å^3	
Z	2	
density (calcd)	8.211 g/cm^3	
absorption coefficient	75.968 mm^{-1}	
F(000)	956	
θ range for data collection	2.18°−24.98°	
index ranges	$-14 \le h \le 14$, $-4 \le k \le 4$, $-11 \le l \le 10$	
reflections collected	2971	
independent reflections	505 [R(int) = 0.1349]	
completeness to θ = 24.98°	100.0%	
refinement method	full-matrix least-squares on F^2	
data/restraints/parameters	505/0/31	
goodness-of-fit on F^2	1.053	
final R indices[a] [$I > 2\sigma(I)$]	R1 = 0.0632, wR2 = 0.1465	
R indices (all data)	R1 = 0.0867, wR2 = 0.1565	
largest diff peak and hole	6.574 and −2.139 e Å^{-3}	

[a] $R = \sum||F_o| - |F_c||/\sum|F_o|$, wR2 = $\{\sum[w(|F_o|^2 - |F_c|^2)^2]/\sum[w(|F_o|^4)]\}^{1/2}$, $w = 1/[\sigma^2(F_o^2) + (0.0809P)^2 + 0.0000P]$, where $P = (F_o^2 + 2F_c^2)/3$.

Pb, Bi, and S are barely resolved near E_F. Our calculations thus indicate a heterostructure-like electronic state for $[Pb_2BiS_3]$-$[AuTe_2]$, which consists of one insulating layer, $[Pb_2BiS_3]$, and one conductive layer, $[AuTe_2]$. The insulating behavior of $[Pb_2BiS_3]$ is rationalized by the fact that it is a valence-precise entity that induces localization of charge carriers, much like in PbS and Bi_2S_3. Although the anionic $[AuTe_2]$ layer is formally also valence-precise, the close Te···Te interchain interactions cause dispersive bands, which give rise to the metallic character in this layer.

The insulating property of $[Pb_2BiS_3]$ can be further understood from the perspective of charge localization. Assuming in-plane currents were applied in this layer, the distorted lattice skews the carrier's trajectory over the length of one Pb−S bond, which is 2.9550(64)−2.9769(23) Å long, as shown in Figure1c, therefore limiting the carriers' mean free path (l) in this distance. According to the Ioffe−Regel criterion, when the l is smaller than the de Broglie wavelength [$\lambda = h/m\nu_F$ (h is the Planck constant, m is the effective mass, and ν_F is the Fermi velocity)], charge carriers are strongly localized, leading to insulating behavior.[12] Given the bare electron mass for a metal and $\nu_F = 1 \times 10^4$ to 1×10^6 m/s for regular solid-state materials, the de Broglie wavelength λ is estimated to be 6−600 Å, far larger than the l in $[Pb_2BiS_3]$. It is worth mentioning that the structure-induced localization effect also occurs in other layered materials, for instance, in $[Tl_4Sb_6Se_{10}]$-$[Sn_5Sb_2Se_{14}]$,[6] indicating a general feature of this class of materials. Figure 3c is a simulation of the Fermi surface (FS). The cylinder-shaped FS agrees with the 2D character of our structure. The FS in the middle of the Brillouin zone is from the hole band and the other two cylinders arise from the electron bands. The cross-section of the electron FS is virtually isotropic, while the hole FS shows a "bow tie" geometry from the c-axis projection. To summarize, the electronic structure of $[Pb_2BiS_3][AuTe_2]$ features two primary characteristics, a multiband metal character and heterostructure nature. These characteristics drastically influence the transport properties.

Transport measurements on single crystals were performed with currents applied in-plane and out-of-plane. As shown in Figure 4a, the in-plane resistivity (ρ_{ab}) decreases with temperature, consistent with metallic behavior and in agreement with the band structure calculations. Interestingly, a slight upturn of ρ_{ab} below 40 K is observed. This anomalous temperature dependence may indicate a possible charge density wave occurring due to Fermi surface nesting between the electron pocket and the hole pocket. Moreover, a difference in temperature-dependent scattering of electrons and holes can also lead to this phenomenon.[13,14] More details of this resistivity anomaly are discussed in the Supporting Information.

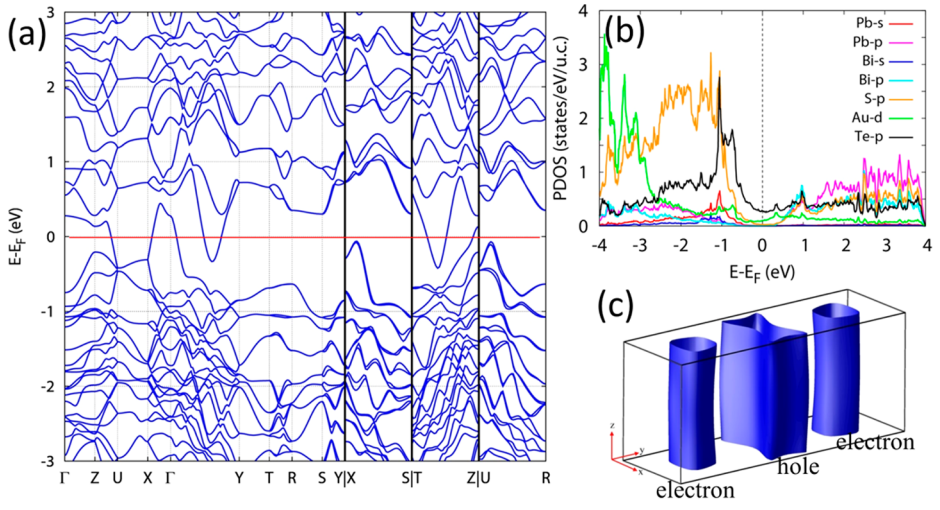

Figure 3. (a) Calculated electronic and structure showing that $[Pb_2BiS_3][AuTe_2]$ is a multiband metal with a hole pocket near X-Γ and two electron pockets near Γ-Y and T-Z, respectively. (b) The density of states plot demonstrates that the dominant contributions near the Fermi surface are the p-orbitals of Te and the d-orbitals of Au atoms. (c) The cylinder-shaped Fermi surface of $[Pb_2BiS_3][AuTe_2]$ exhibits a telltale 2D characteristic.

DOI: 10.1021/ja5111688
J. Am. Chem. Soc. 2015, 137, 2311−2317

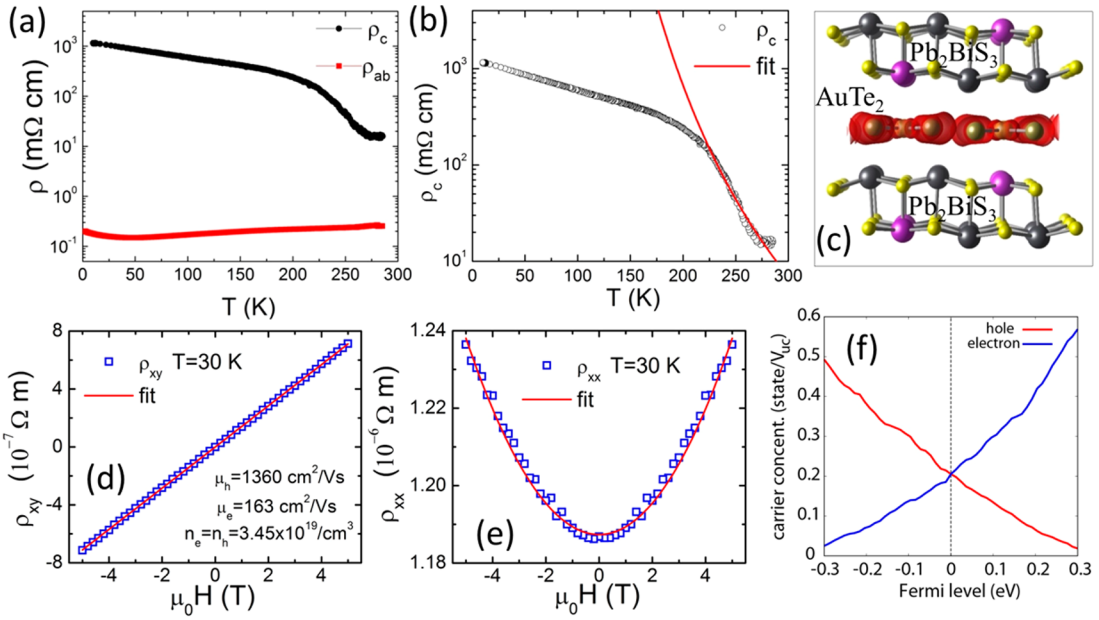

Figure 4. (a) Temperature-dependent resistivity for currents applied in the *ab*-plane and along the *c*-axis, respectively. (b) A fit of the *c*-axis resistivity using the classic activation-type formula. ρ_c deviates from the data below 220 K, indicating a smaller excitation gap at lower temperatures. (c) Side-view of the electron density contour. The electron density near the Fermi level is confined to the single-atom-thick $[AuTe_2]$ layer. (d) In-plane Hall resistivity at 30 K displays linear field dependence. (e) In-plane longitudinal resistivity at 30 K exhibits a B^2 relation, where $B = \mu_0 H$ is the magnetic field. The red solid lines in parts d and e are simulations using the solved transport parameters. (f) Theoretical calculations of the carrier numbers of both electron pockets and hole pocket per unit cell (UC) volume. The number of electrons and holes are identical at the zero energy, indicating the charge compensation property of the undoped $[Pb_2BiS_3][AuTe_2]$.

The out-of-plane resistivity (ρ_c) shows insulating behavior. Its value increases by 2 orders of magnitude from room temperature to 5 K. Therefore, $[Pb_2BiS_3][AuTe_2]$ demonstrates a strikingly large anisotropy ($\Gamma = \rho_c / \rho_{ab} \approx 10^4$) at low temperatures, comparable to that of highly anisotropic graphite and $Bi_2Sr_2CaCu_2O_{6+\delta}$.[15,16] The large ρ_c (in units of Ω cm) indicates a gap opening in the normal direction. Indeed, an energy barrier can be extracted from the temperature-dependent ρ_c. As shown in Figure 4b, the red solid line is a fit using the classic activation-type formula[16] $\rho_c = (a/T) \exp(\Delta/T) + c$, where a and c are fitting parameters and Δ represents the activation energy gap and is 0.21 ± 0.03 eV in our case. This energy gap is fully consistent with the insulating behavior of the $[Pb_2BiS_3]$ layer. To gain a theoretical understanding of the "energy barrier", we simulated the electron density contour and plot it in Figure 4c. It is striking to find that the majority of electrons near the FS accumulate in the $[AuTe_2]$ layer. In contrast, the electron density in the $[Pb_2BiS_3]$ layer is barely resolved. Therefore, the charge carriers must "tunnel" or overcome the energy barrier of the insulating $[Pb_2BiS_3]$ layer to travel along the *c*-axis. The divergence of ρ_c becomes weak below 220 K, indicating a different interlayer conductive process, for example, a smaller activation gap or current leaks due to crystal defects occurring.

Charge carrier transport in the single-atom-thick $[AuTe_2]$ layers is of high interest. A high electrical conduction may be expected because of the simple $[AuTe_2]$ structure and the 2D conducting channels. Magneto-transport on single crystals was thus performed with magnetic fields applied perpendicular to crystal's *ab*-plane. Parts d and e of Figure 4 are field-dependent transverse (ρ_{xy} or Hall resistivity) and longitudinal (ρ_{xx}) resistivity obtained at $T = 30$ K. Contrary to the nonlinear field-dependent ρ_{xy} usually observed in multiband systems, a linear field dependence is observed at 30 K and at other temperatures (see Supporting Information). This anomaly does not contradict the calculated multiband properties of the material. It, however, unveils the compensated two-band nature of the material, where the carrier concentration of electrons equals that of the holes, $n_e = n_h$.[13,14,17]

Another fingerprint of a compensated two-band system is the B^2 relation of ρ_{xx}, which is also satisfied, as shown in Figure 4e.[13,17] Furthermore, the compensated multiband nature is supported by our calculations, giving the same volume for the electron pockets and hole pockets (see below). The three-band material $[Pb_2BiS_3][AuTe_2]$ can be simplified to a two-band system given the degenerate electron bands, and therefore, the classical two-band model can be employed to quantitatively explain the transport behavior.[13] Details of the compensated two-band model are provided in the Supporting Information.

Taking advantage of the compensated carriers and the two-band model, the transport parameters of each band, including n_e, n_h, and the mobility μ_e and μ_h, can be directly solved: $n_e = n_h = 3.45 \times 10^{19}/\text{cm}^3$, $\mu_e = 163$ cm^2/(V s), and $\mu_h = 1360$ cm^2/(V s). The corresponding 2D carrier concentration in each $[AuTe_2]$ layer is $n_{2D} = 3.2 \times 10^{12}/\text{cm}^2$, using the relation $n_{2D} = n_{3D}d$, where n_{3D} equals n_e (n_h) and d is the interlayer $[AuTe_2]-[AuTe_2]$ distance, 0.93 nm.[15] The red solid lines in Figure 4d,e are simulations using the solved transport parameters and they fit the experimental data very well. Moreover, we integrated the reciprocal space of the electron bands and the hole band to obtain the carrier numbers for each band. As shown in Figure 4f, at E_F, the number of carrier electrons is equal to that of holes, providing a theoretical proof of the compensated nature of the undoped $[Pb_2BiS_3][AuTe_2]$.

The room-temperature hole mobility [$\mu_h = 1360$ cm^2/(V s)] is comparable to that of surface electrons of topological insulators.[18−20] Limited by sample quality in this study, the μ_h is far lower than that of graphene and of 2D electron gas at

DOI: 10.1021/ja5111688
J. Am. Chem. Soc. 2015, 137, 2311−2317

semiconductor interfaces.[2,21] Nevertheless, the Fermi velocity (ν_F), which represents the theoretical upper limit of carrier velocity, may indicate its potential for applications in electronics. As shown in Figure 5, the solid curves are the

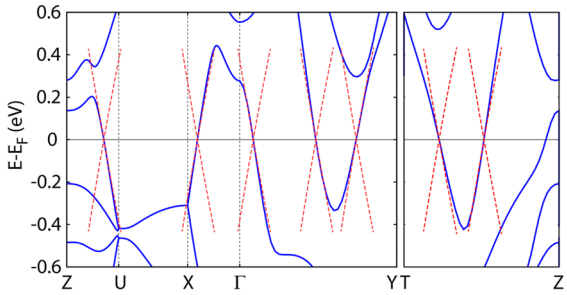

Figure 5. Band structure of $[Pb_2BiS_3][AuTe_2]$ (blue solid curves) with comparison to the Dirac cones of graphene (red dash lines). The overlapping of band dispersion demonstrates the comparable Fermi velocity [$\nu_F = \partial E(k)/\partial k_F$] of both materials.

energy bands of $[Pb_2BiS_3][AuTe_2]$ and the red dashed lines are for the reference material, graphene. Two dashed lines cross each other and form the well-known Dirac cone electronic structure. The bands of $[Pb_2BiS_3][AuTe_2]$ overlap with the branches of the Dirac cone near E_F, leading to a high ν_F that is similar to that of graphene and greater than that of other notable 2D systems, such as MoS_2, germanene, and FeSe.[22−24] High Fermi velocity on the order of 10^6 m/s also occurs in simple metals, for instance, Au and Cu.[13] In this regard, the high ν_F in $[Pb_2BiS_3][AuTe_2]$ is consistent with the relatively simple $[AuTe_2]$ conductive layer.

Because a normal parabolic dispersion is generally expected for materials of this type, the linear dispersions near the Fermi level are unusual. We notice that the FS shows mirror symmetry in the Brillouin zone (Figure 3c) reminiscent of other systems with such symmetry exhibiting exotic mechanisms of symmetry protection[33] in influencing the electronic structure. Furthermore, strong spin−orbit coupling (SOC) from the heavy elements Pb, Bi, Au, and even Te could also impact the linearly dispersive bands, reminiscent of the Dirac cone electronic structure of topological insulators in which SOC takes a dominant role.[34] The calculated ν_F values of $[Pb_2BiS_3][AuTe_2]$ slightly depend on different k-points of the Fermi surface and are 1×10^6 and 0.97×10^6 m/s for electron pockets and hole pocket, respectively (Figure 6). Another important electronic parameter, the effective mass (m^*), can be also extracted from the band dispersion. However, the generally adopted formula[13] $m^* = 1/(\partial^2 E/\partial k^2)$ is not applicable here because the linearly dispersive bands numerically lead to infinite Fermi velocity. Approximately, we choose the values of the edges between the linearly dispersive band and the parabolic one to validate this calculation, although the energy levels of the edges are 0.2 eV away from the Fermi level. The obtained m^* are $0.066m_e$ and $0.046m_e$ for electrons and holes, respectively, where the m_e is the mass of a free electron. These values are comparable to the reported m^* of 2D electrons of graphene, which is $0.01m_e$−$0.06m_e$.[1,21] Presumably, the intrinsic values of m^* should be considerably smaller than our estimation. Direct measurements of ν_F and m^* are beyond our current scope. Nevertheless, the self-consistency of the theory and experiments presented here validates the calculated high Fermi velocities and linear band dispersion.

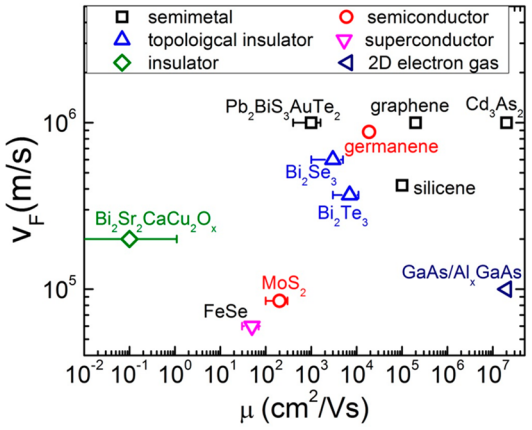

Figure 6. A summary of ν_F and mobility (μ) of different electronic materials. The material parameters of graphene are from ref 21. The values of the Dirac metal Cd_3As_2 are from refs 25 and 26. The parameters of germanene and silicone are reported in refs 23, 27, and 28. The literature on topological insulators Bi_2Se_3 and Bi_2Te_3 is refs 18−20. The material parameters of 2D electron gas are from the review in ref 2. The MoS_2 is referred from refs 22 and 29. The ν_F of bulk crystal FeSe is from ref 24. The mobility of monolayer FeSe thin film was reported in ref 30. The monolayer $Bi_2Sr_2CaCu_2O_x$ is insulating due to the oxygen deficiency.[31] Here we assign a low mobility of less than 1 $cm^2/(V\ s)$. The ν_F of bulk crystal $Bi_2Sr_2CaCu_2O_x$ is from ref 32

CONCLUSIONS

The naturally occurring mineral buckhornite can be synthesized as a single phase with the stoichiometry $[Pb_2BiS_3][AuTe_2]$. It is a unique 2D material with linearly dispersed electronic bands near the Fermi level and compensated electrons and holes confined in single-atom-thick layers. $[Pb_2BiS_3][AuTe_2]$ possesses an extremely large anisotropy ($\Gamma = \rho_c/\rho_{ab} \approx 10^4$), which is comparable to that of benchmark materials, such as graphite and $Bi_2Sr_2CaCu_2O_{6+\delta}$. The electronic structure features linear band dispersion at the Fermi level that leads to projected ultrahigh Fermi velocities of 10^6 m/s, similar to those of graphene. This attractive electronic structure and the good cleavable property of the crystals highlight a novel 2D heterostructured system whose remarkable physical properties should be investigated in more depth in the future.

EXPERIMENTAL SECTION

Crystal Growth and Structure Determination. Single crystals of $[Pb_2BiS_3][AuTe_2]$ were grown using the self-flux method. High-purity Pb nuggets (99.999%, American Elements), Bi powder (99.999%, American Elements), Au powder (99.9999%, Sigma-Aldrich), Te powder (99.999%, American Elements), and S flakes (99.999%, American Elements) were weighted stoichiometrically. The total weight of the starting materials is 1−3 g. These materials were sealed in an evacuated quartz tube in high vacuum (10^{-4} m bar) and subsequently mounted into a tube furnace. The furnace was warmed up to 850 °C in 40 h and dwelled at this temperature for another 2 h. Afterward, the furnace was slowly cooled down to 650 °C in 3 days and then shut off.

Single crystals of $[Pb_2BiS_3][AuTe_2]$ tend to grow horizontally on the surface of the ingot materials. The crystals were planar shaped with dark-golden hues and mirror-like surfaces. The as-grown crystals are generally small and thin (maximum planar size 600 × 600 μm^2 and thickness 5−8 μm). The dominant byproducts of the synthesis are $Pb_{6-x}Bi_{2+x}S_9$, $Pb_3Bi_2S_6$, and $AuTe_2$. Efforts to grow larger crystals via longer cooling times, higher dwelling temperatures, or adding extra

DOI: 10.1021/ja5111688
J. Am. Chem. Soc. 2015, 137, 2311−2317

precursor $AuTe_2$ did not result in significant improvements on crystal size and yield.

Separating the crystals of $[Pb_2BiS_3][AuTe_2]$ from the ingot requires great care, since the crystals are extremely soft and tend to bend, break, or cleave with external force. The lamellar character of the crystals makes it challenging to select crystals suitable for single-crystal X-ray diffraction. Substantial effort, labor, and time were devoted to crystal selection in our studies.

The crystal composition was determined by EDS (Energy Dispersive Spectroscopy) on a Hitachi S-3400N VP-SEM. Single-crystal X-ray diffraction experiments were performed in an IPDS 2T diffractometer at room temperature. The structure was solved by direct methods and refined by full-matrix least-squares on F^2 using the SHELXTL program package. Transmission electron microscopy was performed using a JEOL 2100 F microscope operated at 200 kV.

Transport Characterization. Crystals with thin plate shape (400 × 200 × 5 μm^3) were selected and mounted on insulating glass substrate for transport characterization. For the in-plane magneto-conductance measurements, electrical contacts were fashioned into a Hall-bar geometry. Silver paste was applied by hand on both of the surfaces and the edges to ensure reliable electrical contacts. For the *c*-axis measurements, two separated contacts were painted on both the top and the bottom surface of a crystal. The current contacts were spread over a large area of the cleaved surface to maintain uniform current flow in the normal direction. The voltage contacts were strictly aligned to avoid in-plane conduction. Anisotropy determination was conducted on the same crystal to avoid sample-to-sample differences. Transport measurements were conducted in a LHe^4 variable-temperature cryostat and in a PPMS (Quantum Design).

Band Structure Calculations. The electronic band structures of $[Pb_2BiS_3][AuTe_2]$ were determined with the projector augmented wave (PAW) method and the generalized gradient approximation (GGA) within the Perdew–Burke–Ernzerhof formalism as implemented in the Vienna Ab Initio Simulation Package.[35,36] The energy cutoff for the plane wave basis was set to 350 eV. Momentum space integrations were performed on a 4 × 12 × 6 regular grid for a self-consistent calculation, and the Fermi surface was plotted on a 16 × 48 × 20 regular grid. Spin–orbit coupling was included in a noncollinear scheme.

The electronic band structure of graphene was calculated using the same method (PAW and GGA). Energy cutoff for the plane wave basis was set to 350 eV, and a γ-centered 16 × 16 × 1 regular grid was chosen for momentum space integration in a self-consistent calculation. Our calculations gave $\nu_F \approx 1 \times 10^6$ m/s and fully agree with the reported values in the literature.[21]

■ ASSOCIATED CONTENT

Supporting Information

Details of the crystallographic data, including atomic coordinates, anisotropic thermal parameters, and CIF file, and characterizations and discussions of low-temperature magneto-conductance, the compensated two-band model, theoretical simulations of the planar electron density, and optical images of exfoliated crystals. This material is available free of charge via the Internet at http://pubs.acs.org/.

■ AUTHOR INFORMATION

Corresponding Authors

lei.fang@northwestern.edu
m-kanatzidis@northwestern.edu

Notes

The authors declare no competing financial interest.

■ ACKNOWLEDGMENTS

This research was supported by the Department of Energy, Office of Basic Energy Sciences, under Contract No. DE-AC02-06CH11357. Transmission electron microscopy work was performed in the (EPIC) (NIFTI) (Keck-II) facility of the NU*ANCE* Center at Northwestern University. The NU*ANCE* Center is supported by NSF-NSEC, NSF-MRSEC, the Keck Foundation, the State of Illinois, and Northwestern University.

■ REFERENCES

(1) (a) Novoselov, K. S.; Geim, A. K.; Morozov, S. V.; Jiang, D.; Zhang, Y.; Dubonos, S. V.; Grigorieva, I. V.; Firsov, A. A. *Science* **2004**, *306*, 666–669. (b) Zhang, Y.-B.; Tan, Y.-W.; Stormer, H. L.; Kim, P. *Nature* **2005**, *438*, 201–204. (c) Nixon, D. E.; Parry, G. S.; Ubbelohde, A. R. *Proc. R. Soc. London, Ser. A* **1966**, *291*, 324–339.

(2) For a review, see the following: Ando, T.; Fowler, A. B.; Stern, F. *Rev. Mod. Phys.* **1982**, *54*, 437–672.

(3) For reviews, see the following: (a) Geim, A. K.; Grigorieva, I. V. *Nature* **2013**, *499*, 419–425. (b) Nicolosi, V.; Chhowalla, M.; Kanatzidis, M. G.; Strano, M. S.; Coleman, J. N. *Science* **2013**, *340*, 1226419. (c) For crystal structure of MoS_2, see the following: Dickinson, R. G.; Pauling, L. *J. Am. Chem. Soc.* **1923**, *45*, 1466–1471.

(4) Zhao, L.-D.; Lo, S.-H.; Zhang, Y.; Sun, H.; Tan, G. J.; Uher, C.; Wolverton, C.; Dravid, V. P.; Kanatzidis, M. G. *Nature* **2014**, *508*, 373–377.

(5) (a) Kanatzidis, M. G. *Acc. Chem. Res.* **2005**, *38*, 359–368. (b) Fang, L.; Stoumpos, C. C.; Jia, Y.; Glatz, A.; Chung, D. Y.; Claus, H.; Welp, U.; Kwok, W. K.; Kanatzidis, M. G. *Phys. Rev. B* **2014**, *90*, 020504(R). (c) Nakayama, K.; Eto, K.; Tanaka, Y.; Sato, T.; Souma, S.; Takahashi, T.; Segawa, K.; Ando, Y. *Phys. Rev. Lett.* **2012**, *109*, 236804.

(6) (a) Fang, L.; Iyer, R. G.; Tan, G. J.; West, D. J.; Zhang, S. B.; Kanatzidis, M. G. *J. Am. Chem. Soc.* **2014**, *136*, 11079–11084. (b) Heideman, C. L.; Tepfer, S.; Lin, Q.; Rostek, R.; Zschack, P.; Anderson, M. D.; Anderson, I. M.; Johnson, D. C. *J. Am. Chem. Soc.* **2013**, *135*, 11055–11062. (c) Chiritescu, C.; Cahill, D. G.; Nguyen, N.; Johnson, D. C.; Bodapati, A.; Keblinski, P.; Zschack, P. *Science* **2007**, *315*, 351–353. (d) Gao, Y.; Coppens, P.; Cox, D. E.; Moodenbaugh, A. R. *Acta Crystallogr., Sect. A* **1993**, *49*, 141–148.

(7) Francis, C. A.; Criddle, A. J.; Stanley, C. J.; Lange, D. E.; Shieh, S.; Francis, J. G. *Can. Mineral.* **1992**, *30*, 1039–1047.

(8) Effenberger, H.; Culetto, F. J.; Tapa, D.; Paar, W. H. *Z. Kristallogr.* **2000**, *215*, 10–16.

(9) Pease, R. S. *Acta Crystallogr.* **1952**, *5*, 356–361.

(10) (a) Nixon, D. E.; Parry, G. S.; Ubbelohde, A. R. *Proc. R. Soc. London, Ser. A* **1966**, *291*, 324–339. (b) Li, H.; Wu, J.; Huang, X.; Lu, G.; Yang, J.; Lu, X.; Xiong, Q.; Zhang, H. *ACS Nano* **2013**, *7*, 10344–10355.

(11) (a) Kresse, G.; Hafner, J. *Phys. Rev. B* **1993**, *47*, 558. (b) Kresse, G.; Furthmuller, J. *Phys. Rev. B* **1996**, *54*, 11169.

(12) Ioffe, A. F.; Regel, A. R. *Prog. Semicond.* **1960**, *4*, 237.

(13) Ashcroft, N. W.; Mermin, D. N. *Solid State Physics*; Saunders College Publishing: Philadelphia, PA, 1976.

(14) Fang, L.; Luo, H.; Cheng, P.; Wang, Z.; Jia, Y.; Mu, G.; Shen, B.; Mazin, I. I.; Shan, L.; Ren, C.; Wen, H.-H. *Phys. Rev. B* **2009**, *80*, 104508(R).

(15) Kopelevich, Y.; Torres, J. H. S.; da Silva, R. R.; Mrowka, F.; Kempa, H.; Esquinazi, P. *Phys. Rev. Lett.* **2003**, *90*, 156402.

(16) Watanabe, T.; Fujii, T.; Matsuda, A. *Phys. Rev. Lett.* **1997**, *79*, 2113–2116.

(17) Du, X.; Tsai, S.-W.; Maslov, D. L.; Hebard, A. F. *Phys. Rev. Lett.* **2005**, *94*, 166601.

(18) Xiong, J.; Petersen, A. C.; Qua, D. X.; Hor, Y. S.; Cava, R. J.; Ong, N. P. *Physica E* **2012**, *44*, 917–920.

(19) Xiu, F.-X.; He, L.; Wang, Y.; Cheng, L.; Chang, L.-T.; Lang, M.; Huang, G.; Kou, X.; Zhou, Y.; Jiang, X.; Chen, Z.; Zou, J.; Shailos, A.; Wang, K. L. *Nat. Nanotechnol.* **2011**, *6*, 216–221.

(20) Fang, L.; Jia, Y.; Miller, D. J.; Latimer, M. L.; Xiao, Z. L.; Welp, U.; Crabtree, G. W.; Kwok, W.-K. *Nano Lett.* **2012**, *12*, 6164–6169.

(21) (a) Castro Neto, A. H.; Guinea, F.; Peres, N. M. R.; Novoselov, K. S.; Geim, A. K. *Rev. Mod. Phys.* **2009**, *81*, 109. (b) Allen, M. J.; Tung, V. C.; Kaner, R. B. *Chem. Rev.* **2009**, *110*, 132–145.

DOI: 10.1021/ja5111688
J. Am. Chem. Soc. 2015, 137, 2311–2317

(22) Rose, F.; Goerbig, M. O.; Piéchon, F. *Phys. Rev. B* **2013**, *88*, 125438.
(23) Trivedi, S.; Srivastava, A.; Kurchania, R. *J. Comput. Theor. Nanosci.* **2014**, *11*, 1−8.
(24) Nakayama, K.; Sato, T.; Richard, P.; Kawahara, T.; Sekiba, Y.; Qian, T.; Chen, G. F.; Luo, J. L.; Wang, N. L.; Ding, H.; Takahashi, T. *Phys. Rev. Lett.* **2010**, *105*, 197001.
(25) Liu, Z. K.; Jiang, J.; Zhou, B.; Wang, Z. J.; Zhang, Y.; Weng, H. M.; Prabhakara, D.; Mo, S.-K.; Peng, H.; Dudin, P.; Kim, T.; Hoesch, M.; Fang, Z.; Dai, X.; Shen, Z. X.; Feng, D. L.; Hussain, Z.; Chen, Y. L. *Nat. Mater.* **2014**, *13*, 677.
(26) Liang, T.; Gibson, Q.; Ali, M. N.; Liu, M.; Cava, R. J.; Ong, N. P. *arXiv.org* arXiv:1404.7794 [cond-mat.str-el] (preprint).
(27) Bianco, E.; Butler, S.; Jiang, S.; Restrepo, O. D.; Windl, W.; Goldberger, J. E. *ACS Nano* **2013**, *7*, 4414−4421.
(28) Koski, K. J.; Cui, Y. *ACS Nano* **2013**, *7*, 3739−3743.
(29) Kim, S.; Konar, A.; Hwang, W.-S.; Lee, J. H.; Lee, J.; Yang, J.; Jung, C.; Kim, H.; Yoo, J.-B.; Choi, J.-Y.; Jin, Y. W.; Lee, S. Y.; Jena, D.; Choi, W.; Kim, K. *Nat. Commun.* **2012**, *3*, 1011.
(30) Sun, Y.; Zhang, W.; Xing, Y.; Li, F.; Zhao, Y.; Xia, Z.; Wang, L.; Ma, X.; Xue, Q-K; Wang, J. *arXiv.org* arXiv:1404.3464 [cond-mat.supr-con] (preprint).
(31) Novoselov, K. S.; Jiang, D.; Schedin, F.; Booth, T. J.; Khotkevich, V. V.; Morozov, S. V.; Geim, A. K. *Proc. Natl. Acad. Sci. U. S. A.* **2005**, *102*, 10451−10453.
(32) Deutscher, G. *Rev. Mod. Phys.* **2005**, *77*, 109.
(33) (a) Fu, L. *Phys. Rev. Lett.* **2011**, *106*, 106802. (b) Kane, C. L.; Mele, E. J. *Phys. Rev. Lett.* **2005**, *95*, 226801.
(34) For reviews, see the following: (a) Moore, J. E. *Nature* **2010**, *464*, 194−198. (b) Qi, X.-L.; Zhang, S.-C. *Phys. Today* **2010**, *63*, 33−38. (c) Cava, R. J.; Ji, H. W.; Fuccillo, M. K.; Gibson, Q. D.; Hor, Y. S. *J. Mater. Chem. C* **2013**, *1*, 3176−3189.
(35) Blöchl, P. E. *Phys. Rev. B* **1994**, *50*, 17953.
(36) Perdew, J. P.; Burke, K.; Ernzerhof, M. *Phys. Rev. Lett.* **1996**, *77*, 3865.

DOI: 10.1021/ja5111688
J. Am. Chem. Soc. 2015, 137, 2311−2317